ROTHAMSTED
RESEARCH

Rothamsted Research
Harpenden, Herts, AL5 2JQ

Telephone: +44 (0)1582 763133
Web: http://www.rothamsted.ac.uk/

Algeo, J., Slater, L., Binley, A., Van Dam, R. L. and Watts, C. W. 2018. A comparison of GPR early-time signal approaches for mapping changes in shallow soil water content. *Vadose Zone Journal.* 17 (1), pp. 1-11.

Original Research

Core Ideas

- Early-time amplitude analysis requires understanding of site, system, and methodology.
- The AEA and CFA both have benefits and disadvantages.
- Time window selection is important when shallow reflectors may be present.
- Early time GPR results are highly frequency dependent.

A Comparison of Ground-Penetrating Radar Early-Time Signal Approaches for Mapping Changes in Shallow Soil Water Content

Jonathan Algeo,* Lee Slater, Andrew Binley,
Remke L. Van Dam, and Chris Watts

Improving irrigation efficiency requires accurate assessment of the soil moisture distribution in time and space, but obtaining accurate observational data is challenging. Early-time signal (ETS) amplitude analysis of ground-penetrating radar (GPR) data may permit such rapid noninvasive characterization. In this study we performed controlled irrigation experiments using a multifrequency GPR system to compare two statistics used to quantify the ETS: average envelope amplitude (AEA) and carrier frequency amplitude (CFA). Supporting data were provided by direct measurements, electrical resistivity imaging (ERI), and synthetic modeling. In our first experiment, both statistics successfully related the ETS for 250 and 400 MHz GPR data to increasing water content. However, the 400 MHz AEA lost sensitivity at later stages of the irrigation process, whereas the 400 MHz CFA remained sensitive to changes in water content. The 1000 MHz data did not show the expected relationships, possibly due to shallow reflectors, such as the wetting front, which the higher frequency antennae would have a greater chance of detecting, as supported by synthetic modeling. In our second experiment, we focused on the effect of the time window on calculating ETS statistics. We demonstrate that, when there is interference in the ETS, using a shorter time window instead of the more common first positive half cycle improves correlation with soil moisture content. Our work shows that the GPR ETS data respond to changes in soil water content in similar fashion to ERI data.

Abbreviations: AEA, average envelope amplitude; CFA, carrier frequency amplitude; ERI, electrical resistivity imaging; ETS, early-time signal; FPHC, first positive half cycle; GPR, ground-penetrating radar; GWC, gravimetric water content

The hydrological processes in the vadose zone are important for a wide variety of research topics, including climate modeling, contaminant transport, biological and chemical processes, and agricultural water management (Holden and Fierer, 2005; Nielsen, 1986; Seneviratne et al., 2010). Determining the distribution and dynamics of water in the near surface is therefore a critical component of these research topics. Direct measurements of water content are invasive, labor intensive, and usually impractical at the sampling densities required to reliably capture the complex dynamics of moisture transport in the vadose zone. Noninvasive geophysical sensing of the subsurface can support direct observations by providing spatially extensive proxy measures of moisture content over changes in time (Binley et al., 2015).

Ground-penetrating radar (GPR) is a powerful geophysical method for moisture content monitoring because the dielectric permittivity obtained from the measurement is strongly controlled by volumetric water content (Huisman et al., 2003). Traditional GPR methodologies, such as reflection analysis and ground-wave analysis, have long been successfully used for mapping and monitoring variations in subsurface water content (Huisman et al., 2003). For example, these approaches have been used to study seasonal soil moisture dynamics (Steelman and Endres, 2010) and progression of infiltration fronts (Allroggen et al., 2015). Through the use of multi-offset equipment, it is possible to simultaneously estimate soil moisture and obtain structural information (Mangel et al., 2012).

J. Algeo and L. Slater, Dep. of Earth and Environmental Sciences, Rutgers–State Univ. of New Jersey, Newark, NJ 07102; A. Binley, Lancaster Environment Centre, Lancaster Univ., Lancaster LA1 4YQ, UK; R.L. Van Dam, Dep. of Civil Engineering, Centro Federal de Educação Tecnológica de Minas Gerais, Civil Engineering (CEFET-MG), Belo Horizonte, Minas Gerais, Brazil, and Dep. of Earth and Environmental Sciences, Michigan State Univ., East Lansing, MI 48824; C. Watts, Rothamsted Research, Harpenden, Hertfordshire, AL5 2JQ, UK. *Corresponding author (jonathan.algeo@gmail.com).

Received 2 Jan. 2018.
Accepted 27 June 2018.

Citation: Algeo, J., L. Slater, A. Binley, R.L. Van Dam, and C. Watts. 2018. A comparison of ground-penetrating radar early-time signal approaches for mapping changes in shallow soil water content. Vadose Zone J. 17:180001. doi:10.2136/vzj2018.01.0001

Ground-penetrating radar early-time signal (ETS) amplitude analysis, first introduced by Sbartaï et al. (2006) and Pettinelli et al. (2007), is an alternative to reflection and ground-wave–based GPR surveys for acquiring information on spatial variation in soil dielectric properties in the shallow subsurface (Algeo et al., 2016; Comite et al., 2014; DiMatteo et al., 2013; Ferrara et al., 2013a, 2013b; Pettinelli et al., 2007, 2014). By analyzing the changes in the ETS, defined as the overlapping air- and ground-waves, rather than reflections or the isolated ground-wave, early-time analysis potentially provides information on shallow moisture content variation in environments where GPR is traditionally not a viable tool. Environments where ETS analysis can provide additional information include clay-rich sites with excessive electromagnetic wave attenuation preventing detection of reflected waves, sites with no subsurface reflectors within the depth of penetration, and sites where the ground-wave cannot be practically isolated from the air-wave (Algeo et al., 2016).

Early-time signal amplitude analysis is based on a dimensionless measure of the earliest portion of the GPR signal. The resulting amplitude values are arbitrary, varying based on field site, GPR system, and antenna frequency, in addition to physical changes in the subsurface, such as a change in water content. A clear limitation of the method is that it currently does not provide a quantitative measure of any physical property. Two statistics have been used to quantify the ETS: average envelope amplitude (AEA) (Pettinelli et al., 2007) and carrier frequency amplitude (CFA) (Comite et al., 2016). Earlier research has also investigated the peak-to-peak amplitude of the direct signal (Sbartaï et al., 2006). The AEA statistic, the inverse of which is usually presented (AEA^{-1}) so that it increases with water content, has been shown to correlate with changes in both relative dielectric permittivity (ε_r) and electrical conductivity (σ) (Comite et al., 2014; Pettinelli et al., 2007). The CFA statistic was recently introduced by Comite et al. (2016). They conclude that CFA relates amplitude changes in the ETS to changes in dielectric properties more consistently over a wide range of σ and ε_r values relative to AEA but acknowledge the need for further investigation of CFA in practical applications.

Early-time signal amplitude analysis remains poorly developed relative to more traditional GPR methodologies for subsurface moisture content estimation, such as ground-wave and reflection-based GPR analysis. Previous numerical modeling has suggested that the first positive half cycle (FPHC) of the ETS provides the best signal-to-noise ratio as compared with (i) the first half cycle, which is the portion of the signal from first onset to first negative peak; (ii) all 4-ns time windows between 0 and 12 ns after first arrival for a 250 MHz system (Pettinelli et al., 2007); and (iii) the portion of the signal from first arrival to first positive peak (DiMatteo et al., 2013). However, it is not clear if this represents the best time window for early-time analysis over a wide range of physical conditions. Furthermore, the wavelength of the ETS needs to be considered when performing amplitude analysis because it affects the depth of investigation of the measurement. Choice of wavelength is also an important consideration in ETS analysis when shallow subsurface reflectors may interfere with the ETS because higher-frequency (shorter wavelength) GPR signals are more likely to detect thin and/or shallow reflectors, whereas lower-frequency GPR signals can sample deeper layers and potentially include reflections from deeper interfaces.

Because the ground-wave is a significant portion of the ETS, the depth of investigation of the ETS should be similar to that of the ground-wave (Pettinelli et al., 2014). Models and experimental evidence for the depth of investigation of the ground-wave predict values ranging from 0.17 to 0.6 times the wavelength (Du, 1996; Galagedara et al., 2003; Grote et al., 2003; Sperl, 1999; van Overmeeren et al., 1997). However, further work is needed to determine the true ETS investigation depth as well as the physical controls on it.

This work explores how data acquisition and processing procedures affect the interpretation of ETS measurements. We conducted a field study at a well-characterized site, allowing for assessment of the ETS as a function of antenna frequency and processing methodology. We seek to corroborate previous research and to demonstrate the viability of ETS analysis for providing qualitative information on spatial variations in soil moisture while comparing the CFA and AEA statistics under field conditions. We investigate the impact of antenna frequency and post-processing approach on the resulting interpretation.

Background

Early-Time Ground-Penetrating Radar Amplitude

Unlike reflection- and transmission-based GPR methods, which record changes in travel time of reflected or direct waves, GPR early-time analysis is sensitive to changes in the amplitude of the overlapping air- and ground-waves, which travel directly through the air and ground from the transmitting antenna to the receiver. Sbartaï et al. (2006) initially showed the sensitivity of the ETS to changes in both σ and ε_r. DiMatteo et al. (2013) and Ferrara et al. (2013a) demonstrated through numerical modeling and field study, respectively, that the air-wave ($A_{\text{air-wave}}$) and ground-wave ($A_{\text{ground-wave}}$) amplitudes are related to the electromagnetic properties of the subsurface and the antenna separation (S) by

$$A_{\text{air-wave}} = \frac{\sqrt{\varepsilon_0\mu_0}}{2\pi\varepsilon_0\left(\varepsilon_r - 1\right)S^2} \qquad [1]$$

$$A_{\text{ground-wave}} = -A^0_{\text{ground-wave}} \exp\left[-\left(\frac{1}{2}\right)\frac{\sqrt{\mu_0}}{\varepsilon_0\varepsilon_r}\sigma S\right] \qquad [2]$$

and

$$A^0_{\text{ground-wave}} = \frac{\sqrt{\varepsilon_r\mu_0}}{2\pi\varepsilon_0\left(\varepsilon_r - 1\right)S^2} \qquad [3]$$

where μ_0 is the magnetic permeability of free space, ε_0 is the dielectric permittivity of free space, and A^0 is the amplitude of the ground wave in a vacuum. The exponential term in Eq. [2]

represents the evanescent portion of the ground-wave (Annan, 1973; Di Matteo et al., 2013). Equations [1], [2], and [3] describe the sensitivity of ETS amplitude to changes in ε_r and σ. DiMatteo et al. (2013) showed via numerical simulation that AEA and ε_r remain correlated even under conditions of changing σ, thereby lending support for the interpretation of ETS amplitudes in terms of soil moisture content, which in turn has a strong dependence on ε_r.

Methods

Site Description

Field-based ETS measurements were acquired on Butt Close (52.0119N, 0.5976E), Woburn Experimental Farm, Bedfordshire, UK, which has been operated by Rothamsted Research for almost 100 yr. The experiments described here were performed on a grass field plot with a well-defined soil profile characterized locally as Cottenham Series, which is a coarse-textured brown sand (Catt et al., 1975). This soil is classified internationally as a Cambic Arenosol (IUSS Working Group WRB, 2015). A shallow (~40 cm deep), thin (2–3 cm), iron-rich cemented layer separates an upper, tilled layer from a deeper layer. There was a slight slope of ~2 to 3° downhill toward the start of the transect (meter zero). Measurements were acquired over a 16- by 5-m open area that was devoid of surface features that could generate unwanted reflection events (Fig. 1).

Irrigation Procedure

Data collection occurred during two different field campaigns: 26 July 2016 (Exp. 1) and 5 Aug. 2016 (Exp. 2). For both campaigns, we performed an irrigation experiment coupled to early-time GPR data acquisition.

A 5- by 5-m plot in the middle of the transect was irrigated immediately after background data collection during Exp. 1 and 2. This represents approximately one-third of the length of the line, allowing for two similar-length control areas where no irrigation was performed located on either side of the irrigated area. The irrigation was extended 2.5 m perpendicular to the line in both directions to make the experiment quasi two-dimensional. The plot was irrigated with ~14 L of water per m^2 in each irrigation (equivalent to 14 mm of rain). Approximately 90 min elapsed between each of the three irrigation events in Exp. 1 and between each of the four irrigation events in Exp. 2.

Ground-Penetrating Radar Data Acquisition and Processing

In Exp. 1 and 2, a 16-m GPR line was collected along the same line as the electrical resistivity imaging (ERI) survey described below. Ground-penetrating radar data were collected before the first irrigation and after every subsequent irrigation. An Utsi Electronics GroundVue3 eight-channel, shielded GPR system was used to acquire 250, 400, and 1000 MHz data simultaneously in Exp. 1. This experiment revealed unexpected results in the 1000 MHz GPR data, with the ETS statistics responding opposite to expectations, due to either insensitivity to the irrigation or other factors, such as shallow reflections. Experiment 2 was consequently specifically performed to recollect 1000 MHz data at a temporal sampling rate 8 times higher than in Exp. 1 to permit a more detailed analysis of each early-time trace. The transmitting antenna–receiver spacings were 36 cm for the 250 MHz, 20 cm for the 400 MHz, and 12 cm for the 1000 MHz antennae. The three antennae were arranged side-by-side, with each oriented parallel to the direction of the line, on a plastic sled that was ~80 cm wide.

The GPR surveys consist of ~5600 individual measurements for each irrigation. A preprocessing step, as described in Algeo et al. (2016), was applied, whereby a moving average filter with a window length of seven traces was used to minimize the impacts of outliers likely related in part to variable coupling between antennae and the ground. We did not apply common postprocessing to the GPR data, such as time-zero correction or dewow, because they do not have a relevant effect on the ETS.

The AEA^{-1} statistic was calculated using the Pettinelli et al. (2007) methodology. Each averaged trace was passed directly into MATLAB's native Hilbert transform function. Then, for Exp. 1, the FPHC of the transformed traces was extracted. Taking the absolute value of this resulting portion of the trace gives the envelope of the signal. The integral of the envelope over the time window of the FPHC is then averaged to give the AEA statistic, as per Pettinelli et al. (2014). The inverse AEA values, AEA^{-1}, are plotted and used for analysis so that values increase with increasing permittivity (water content).

The CFA statistic was calculated using the methodology of Comite et al. (2016). The FPHC of each trace was extracted and passed through a fast Fourier transform using MATLAB's native fast Fourier transform function. The absolute value of this result gives the amplitude spectrum of the signal, and the peak amplitude

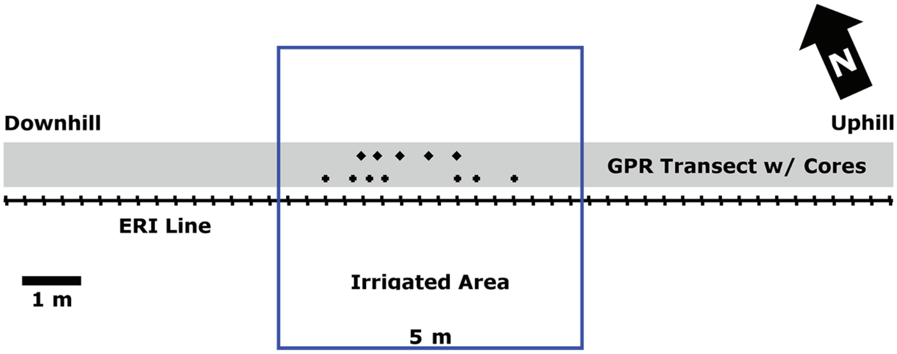

Fig. 1. Map-view schematic of measurement configuration. The black line is the electrical resistivity imaging (ERI) line, with hash marks indicating the 48 electrode locations (32 cm spacing). The gray area represents path of the ground-penetrating radar (GPR) sled. Pluses and diamonds represent soil sample locations from Exp. 1 and 2, respectively. The blue box represents the irrigated area.

of this spectrum is the CFA statistic. For consistency with the AEA statistic, CFA values were then converted to CFA^{-1} values that increase with increasing water content.

The same processing methodology was applied to the dataset acquired in Exp. 2, with the exception that the FPHC of each trace was analyzed in more detail by breaking it into three different-sized portions: the first-third, the first two-thirds, and the entirety of the FPHC (Fig. 2). This was not done with the GPR data from Exp. 1 because measurements were not collected at the necessary higher sampling rate used in Exp. 2. For each portion of the FPHC, AEA^{-1} and CFA^{-1} were calculated independently to analyze how the time window selection affects the two statistics, especially in the context of potential early-time reflectors, which were suspected to have affected the 1000 MHz ETS in Exp. 1. We also calculated the ETS statistics for 10 time windows, representing 10 to 100% of the FPHC, in 10% increments to better visualize which portions of the ETS might contain valuable information.

Electrical Resistivity Imaging Data Acquisition and Processing

In Exp. 1, collection of supporting data began with ERI measurements under "dry," unirrigated conditions. Electrical resistivity imaging data were collected using an IRIS Syscal Pro with 48 electrodes spaced 32 cm apart to provide an approximate imaging depth of 1 m. A total of 316 measurements were collected per profile, using a dipole-dipole geometry. Reciprocal measurements, where the potential and current electrodes are transposed, were collected for each profile to characterize data errors and remove outliers. Electrical resistivity imaging data were inverted using the R2 code (http://www.es.lancs.ac.uk/people/amb/Freeware/R2/R2.htm; see also Binley [2015]). The inversion was discretized to provide a resistivity approximately every 16 cm laterally and approximately every 5 cm vertically. As a result of the smoothing inherent to the inversion process, a conservative estimate of the horizontal resolution of the ERI measurements would be the electrode spacing (32 cm). This resolution decreases with depth, but we are only concerned with the very shallow subsurface sensed with the ETS. The small electrode rods used for ERI data collection were removed prior to GPR data collection and carefully returned to the holes afterward for the next ERI survey.

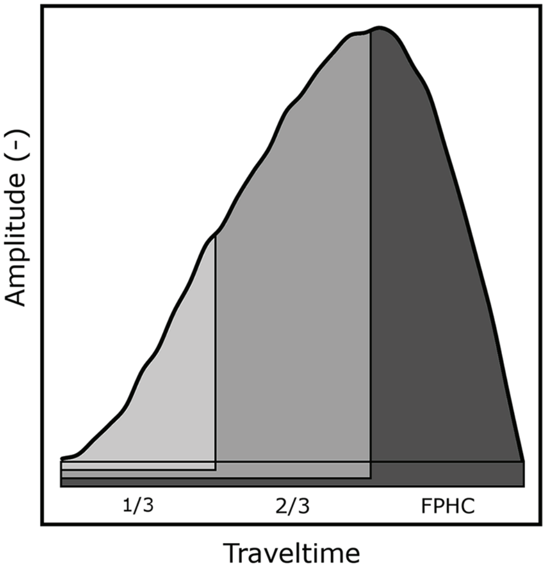

Fig. 2. The three time windows analyzed for Exp. 2 (see Fig. 7). The AEA^{-1} and CFA^{-1} (i.e., the inverse of the average envelope amplitude and the carrier frequency amplitude, respectively) statistics were calculated for the first third of the first positive half cycle (FPHC), the combined first and second thirds, and the entire FPHC.

Soil Coring and Analysis

One soil core was collected prior to irrigation in the target irrigation area. After each irrigation, two soil cores were collected in the irrigated area. The cores were collected to 70 cm depth in 10-cm segments using a 21-mm gouge auger. Cores were promptly sealed in airtight bags and refrigerated until measurements were performed. The gravimetric water content (GWC) of the cores was measured using a standard oven-drying methodology (Klute, 1965).

Soil coring and ERI were performed after each irrigation to provide the independent data on moisture content distribution needed to constrain the interpretation of ETS results.

The same basic procedure was followed in Exp. 2, except that soil cores were collected to only 30 cm depth because, based on Exp. 1, the 1000 MHz antennae were not expected to provide relevant information below this depth, which is significantly greater than the approximate wavelength of a 1000 MHz signal in soil. Additionally, only one core was collected per irrigation event during Exp. 2.

Comparison with Soil Moisture Measurements

We correlated the multifrequency GPR AEA^{-1} and CFA^{-1} values with the soil core GWC and ERI values to demonstrate that relationships can be developed to relate the GPR ETS to soil moisture content. The relative changes after each irrigation event were estimated by dividing the measured GPR, GWC, and ERI values by the values collected under background conditions for all measurements collected in the irrigated region (5–10 m along the transect). We then performed least-squares regression and assessed the quality of the relationships. The soil core GWC 0- to 10-cm data from Exp. 1 and 2 were compared with averaged AEA^{-1} and CFA^{-1} values calculated from 10-cm portions of GPR data centered on each soil core. The 250 MHz GPR data from Exp. 1 were analyzed using the full FPHC, and the 1000 MHz GPR data from Exp. 2 were analyzed using the first half of the FPHC, which we found to provide the best quality data in Exp. 2. We selected resistivity values from a depth of 12.5 cm to limit potential artifacts in the inversion caused by the electrodes and compared them with averaged 16-cm sections of the GPR data.

Synthetic Modeling

We created a synthetic model in gprMax (Warren et al., 2016) to investigate the potential for shallow reflectors to interfere with the GPR ETS of 1000 MHz antennae. The modeled space is a 30- by 40- by 30-cm box. There is a bottom layer of dry soil with an ε_r

of 4 and an electrical resistivity of 400 Ω m. We simulated a top wetted layer increasing in thickness from 0 to 10 cm in 1-cm increments. The wetted soil has an ε_r of 20 and an electrical resistivity of 350 Ω m. Above the wetted layer is 10 cm of free space. We used a Ricker wavelet source with a frequency of 1000 MHz, which was centrally located at the surface of the soil, and offset the same distance from the receiver (12 cm) as the 1000 MHz antenna we used in the field. The time window for the simulation is 20 ns.

Results

Soil Moisture Changes

Figure 3 shows the results of the GWC analysis of the soil cores collected in Exp. 1 and 2. In Exp. 1, the background GWC of the top 10 cm of the subsurface was ~8%, increasing with each irrigation to ~14% after the final irrigation. An increase of 2 to 4% GWC was observed in all core samples taken in the upper 50 cm of the soil. In Exp. 2, the GWC of the top 10 cm of the subsurface increased from 11 to 17% from the first to final irrigation event, with the GWC from 10 to 30 cm remaining relatively unchanged until the final irrigation event, with the exception of a 6% increase from background after the second irrigation, possibly indicative of a preferential flow path in the area of that core.

Figure 4 shows the ERI survey results for Exp. 1. The top image shows the background resistivity structure, characterized by a high-resistivity layer near the surface, above the cemented layer. The resistivity of this layer is in the range of 300 to 400 Ω m, extending to between 0.5 and 1 m depth. The resistivity below the cemented layer is <200 Ω m, extending to the maximum depth of investigation. The lower three plots show relative change from background resistivity after irrigation. These plots show decreasing resistivity, indicating increasing moisture content after subsequent irrigations, and show that the wetting progresses to greater depth with each event. The ERI data in Exp. 2 are similar, with a marked decrease in background resistivity after each irrigation step (data not shown). In both cases, the ERI shows that the resistivity of the subsurface decreased relatively uniformly over the entire length of the irrigation and that the change in resistivity (and, by extension, moisture content) was primarily constrained to the targeted central third of the survey line. The time-sequence of ERI data also showed that the thickness of the wetted layer increased in a fairly uniform fashion.

Analysis of Frequency Impact on Early-Time Signal from Experiment 1

Figure 5 shows the ETS, represented by AEA^{-1} and CFA^{-1}, over the three antenna frequencies used in Exp. 1,

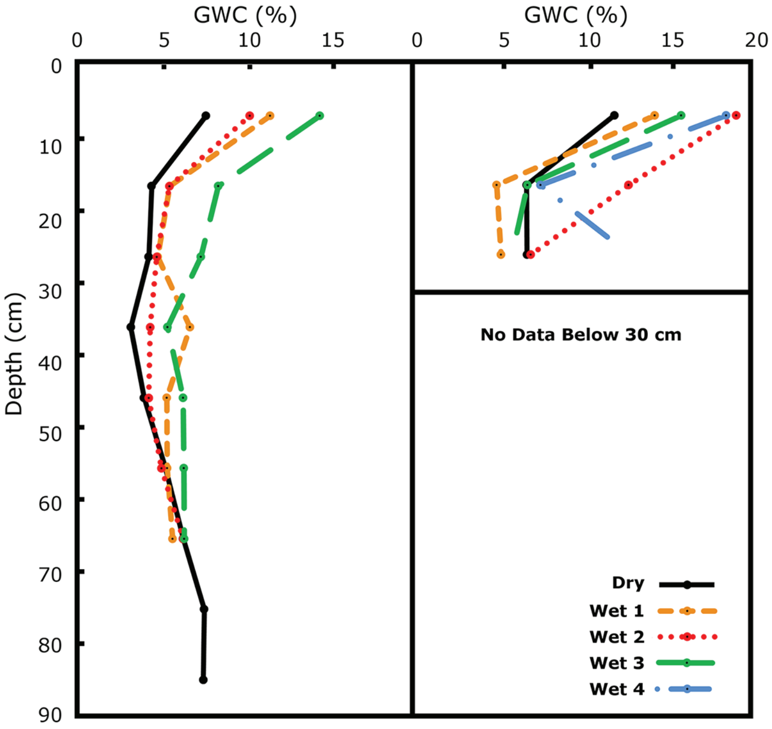

Fig. 3. Gravimetric water content (GWC) analysis of soil cores from Exp. 1 (a) and Exp. 2 (b). Wet 3 and Wet 4 represent the final datasets collected in each experiment.

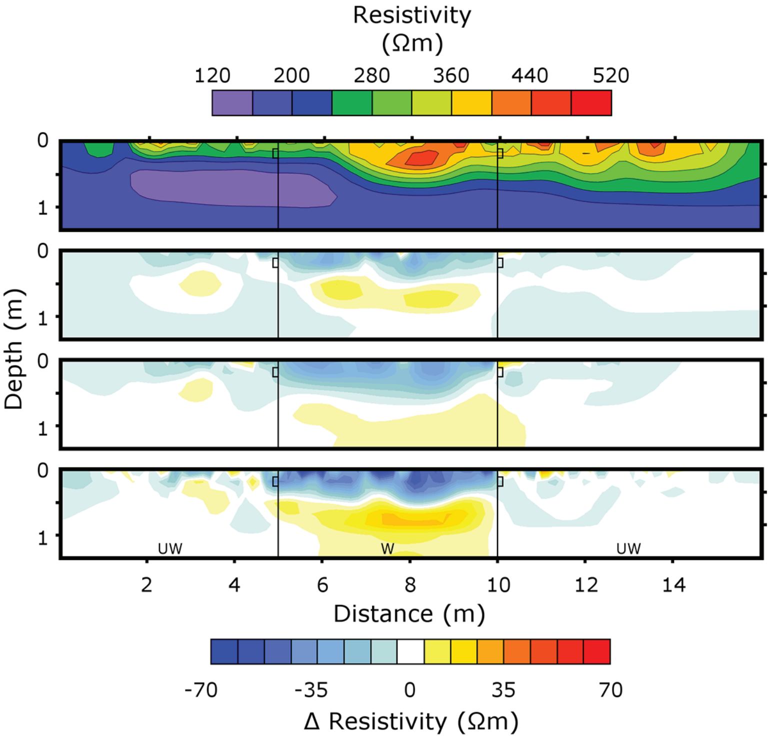

Fig. 4. Experiment 1 electrical resistivity imaging (ERI) results. Resistivity data (a) collected prior to irrigation. (b–d) Different inversion results representing the relative change in resistivity after each irrigation step. UW and W represent the unwetted and wetted areas, respectively. The field site slopes slightly (~2–3°) toward 0 m. The bracketed region (17 cm high, 5 m wide) shows the approximate portion of the ERI data used for correlation with the GPR early-time signal (see Fig. 9).

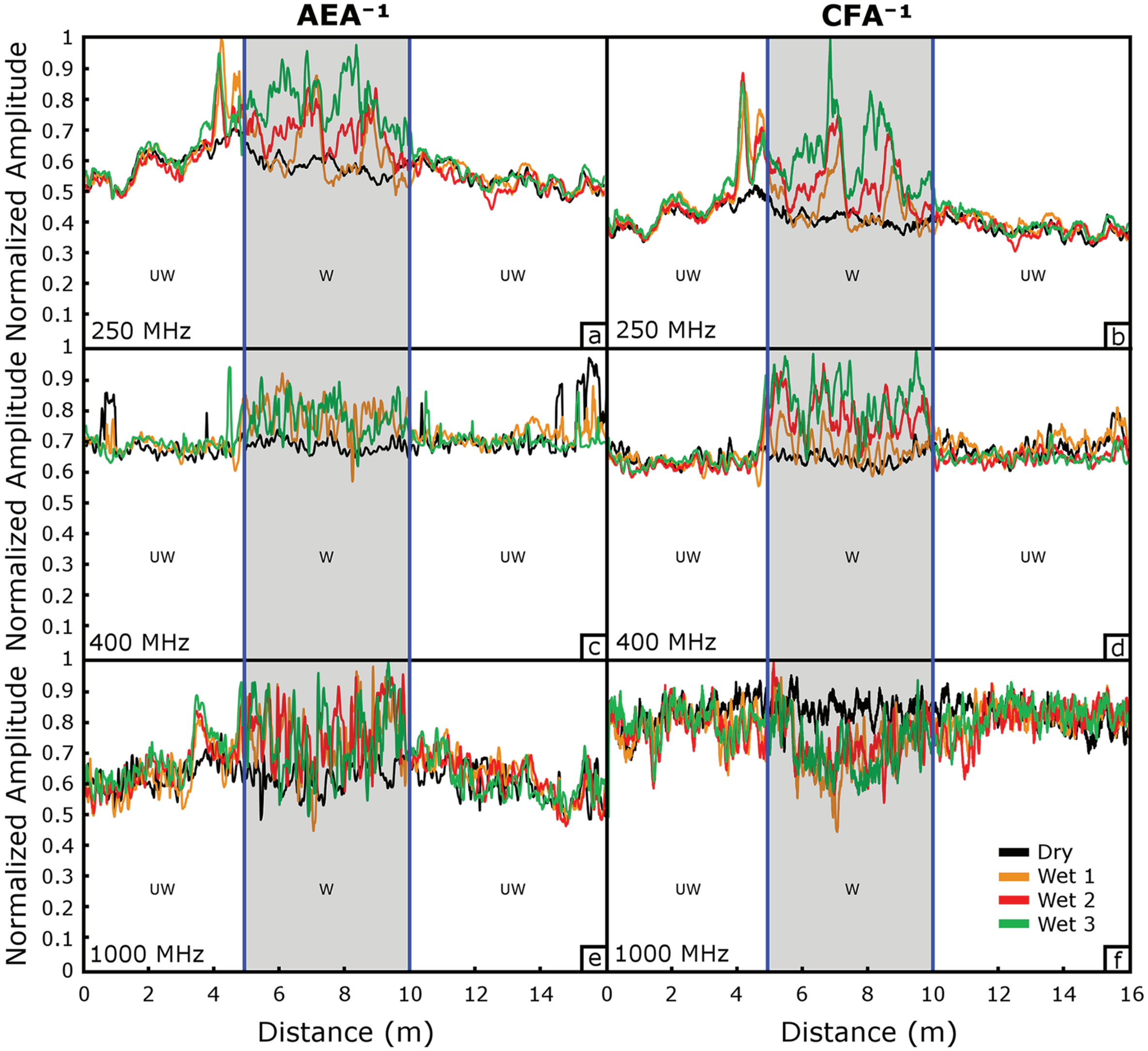

Fig. 5. Experiment 1 early-time ground-penetrating radar data for all frequencies and both early-time signal statistics. Uphill is to the right. The second irrigation dataset was removed from the 400 MHz inverse average envelope amplitude (AEA^{-1}) plot due to significant noise. All values are normalized so that the maximum value for each subplot is 1. Shaded area is the wetted area, additionally marked “W”; the unwetted area is marked “UW.” Black, background data; gold, first irrigation; red, second irrigation; green, third irrigation. Vertical bars delineate the irrigated portion of the line.

with different data series representing different irrigation events. Table 1 shows how the AEA^{-1} and CFA^{-1} values change over time in each of the three portions of the transect. The irrigated portion is considered to extend from 5 to 10 m. Although water was only applied from 5 to 10 m, because of the slight slope at the site, we expect some downhill flow of the irrigation water, as seen in the data. Because of this, we calculate the downhill and uphill control area values on 0 to 4 m and 11 to 15 m, respectively, allowing for a 1-m buffer zone between the control areas and irrigated area. We expect increases in GWC to cause an increase in our AEA^{-1} and CFA^{-1} values. The amplitude values are dimensionless and normalized so that the highest measured value for each frequency/statistic combination is set to one. The higher-frequency GPR data show more significant small-scale variations, presumably because they are sensitive to a smaller volume of the subsurface and are more affected by surface roughness and variations in vegetative cover.

The 250 MHz AEA^{-1} values within the irrigated area increase from a background average of 0.6 to multiple values ranging between 0.7 and 0.95. By the final irrigation, all parts of the irrigated area are between 0.7 and 0.95. The 400 MHz AEA^{-1} values increase from a background value of ~0.7 to between 0.8 and 0.9 throughout the irrigated area. These values reach their peak and remain constant after the first irrigation. The 1000 MHz AEA^{-1} values also peak after one irrigation, increasing from background values of ~0.65 to between 0.8 and 1.0 in the irrigated area. In all cases, the AEA^{-1} values change significantly less outside of the irrigated area. In the 250 MHz AEA^{-1} data, for example, the values change, on average, from background to the final irrigation by 4.82% in the downhill control area, 28.55% in the irrigated area, and 0.67% in the uphill control area (Table 1). The increase in the downhill area is likely due to a small amount of overland flow.

The 250 MHz CFA^{-1} values increased in response to the first irrigation but only in a few locations, where the values jump from background values of ∼0.45 to between 0.6 and 0.8. They continued to increase in a stepwise manner with each irrigation, and by the final irrigation the entire irrigated area had increased from background to between 0.6 and 1. The 400 MHz CFA^{-1} values increased slightly in response to the first irrigation from ∼0.7 to ∼0.8. By the final irrigation, the values averaged ∼0.85 throughout the irrigated area. Contrary to expectations, the 1000 MHz CFA^{-1} data decreased (rather than increase) from background values of ∼0.8 to values, averaging ∼0.65 over successive irrigation events. This finding is further explored in Exp. 2 and by performing synthetic modeling. As with the AEA^{-1} data, by the end of the experiment, changes in the CFA^{-1} data were more significant in the irrigated area (250 MHz: 41.36%; 400 MHz: 22.79%) than in the uphill control area (250 MHz: 3.23%; 400 MHz: −4.42%) or downhill control area (250 MHz: 10.08%; 400 MHz: −0.98%).

Table 1. Data from Experiment 1 showing background CFA^{-1} and AEA^{-1} (inverse of the average envelope amplitude and the carrier frequency amplitude, respectively) values and the change from background (Δ%) for each irrigation and for all combinations of antenna frequency and portion of the line: downhill control area (0–4 m), irrigated area (5–10 m), and uphill control area (11 m to end of line). We excluded the 4 to 5 m and 10 to 11 m portions of the data from the downhill and uphill control areas, respectively, due to evidence that minor overland flow and/or preferential flow was causing water to infiltrate beyond the boundaries of the control area.

Antenna frequency and line portion	Dry	Wet 1	Wet 2	Wet 3
		Δ%		
1000 AEA^{-1}				
Downhill	0.632	−0.24	2.89	6.53
Irrigated	0.634	16.38	20.23	18.42
Uphill	0.590	2.88	1.43	−0.49
1000 CFA^{-1}				
Downhill	0.823	−2.99	−3.95	−2.12
Irrigated	0.852	−13.98	−12.87	−13.71
Uphill	0.817	1.51	2.29	3.08
400 AEA^{-1}				
Downhill	0.692	−0.02	−0.07	0.00
Irrigated	0.693	11.14	3.41	11.42
Uphill	0.744	−2.01	2.88	−4.99
400 CFA^{-1}				
Downhill	0.646	−0.96	−2.91	−0.98
Irrigated	0.656	5.01	16.72	22.79
Uphill	0.687	1.59	−4.36	−4.82
200 AEA^{-1}				
Downhill	0.594	1.57	−0.13	4.82
Irrigated	0.601	8.02	14.64	28.55
Uphill	0.528	1.14	−1.36	1.57
200 CFA^{-1}				
Downhill	0.424	6.42	5.92	10.08
Irrigated	0.425	12.52	24.65	41.36
Uphill	0.373	3.33	−0.06	3.09

Synthetic Model

The results of the synthetic modeling are shown in Fig. 6a. We present the GPR signal from 0 to 5 ns, which includes the entire ETS, as well as reflections created by the modeled wetted layer. These reflections are highlighted by the arrows in Fig. 6a and occur later in time the deeper the wetted layer progresses. When the wetted layer is thinnest, the reflection causes interference with the ETS. In the case of the 1-cm reflection, the shape of the FPHC is changed, which has a significant effect on calculated AEA^{-1} and CFA^{-1} values (Table 2).

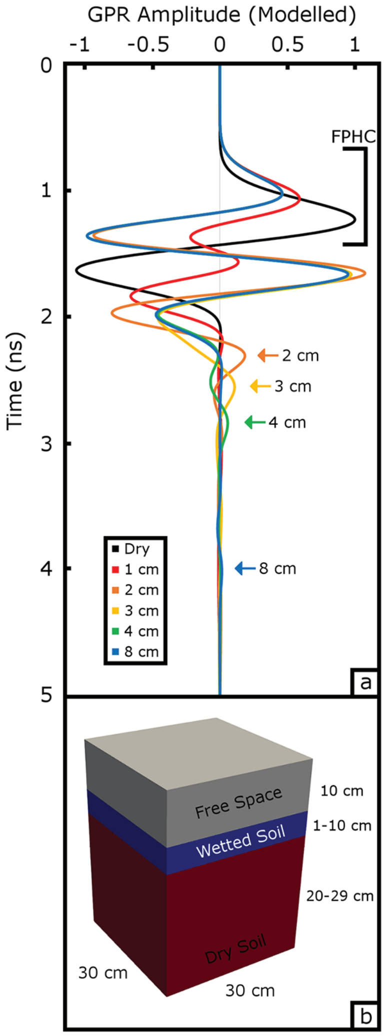

Fig. 6. Results of a synthetic modeling experiment (a) and the three-dimensional geometry of the modeled environment (b). We present the traces from a 1000 MHz antenna placed at the center of the soil surface, with one trace each for five different wetted layer thicknesses: 1 cm (red), 2 cm (orange), 3 cm (yellow), 4 cm (green), and 8 cm (blue). The extent of the first positive half cycle (FPHC), on which early-time signal (ETS) amplitude analysis was performed, is shown. Reflection events caused by the wetting front are highlighted by arrows for wetted layer thicknesses of 2 to 8 cm. The reflection caused by the 1-cm-thick wetted layer interferes with the ETS and cannot be precisely located visually. GPR, ground-penetrating radar.

Table 2. Results of amplitude analysis on the full first positive half cycle of the modeled traces (Fig. 6) for wetted layers from 1- to 8-cm depth.

Inverse amplitude	1 cm	2 cm	3 cm	4 cm	8 cm
AEA^{-1}	2.5053	3.1497	3.1531	3.1532	3.1556
CFA^{-1}	0.0100	0.0147	0.0148	0.0148	0.0148

Impact of Time Window Length on Early-Time Signal from Experiment 2

Figure 7 shows the 1000 MHz CFA^{-1} and AEA^{-1} data collected before irrigation and after the first and the final irrigations in Exp. 2. When processed using the first one-third of the FPHC as the time window, both the AEA^{-1} (Fig. 7a) and CFA^{-1} (Fig. 7b) values increase in the irrigated area after irrigation. When calculated based on the first two-thirds of the FPHC, AEA^{-1} (Fig. 7c) and CFA^{-1} (Fig. 7d) increase, albeit less consistently than the one-third analysis. When ETS analysis is performed on the full FPHC, as is most commonly done, AEA^{-1} (Fig. 7e) and CFA^{-1} (Fig. 7f) decrease in the irrigated area. This is inconsistent with the theory and is the same behavior originally observed in the 1000 MHz data from Exp. 1.

Figure 8 presents an alternate visualization of the 1000 MHz CFA^{-1} and AEA^{-1} data. Early-time signal analysis was performed on cumulative 10% increments of the FPHC, ranging from 20 to 100%. Analyzing only the first 10% of the FPHC did not provide meaningful information. In both the AEA^{-1} and CFA^{-1} data, once we analyze >60% of the signal, the background value begins to decrease significantly, and there is a minimal or negative response of the GPR ETS signal to irrigation. The ETS results cluster for the irrigated events more in the AEA^{-1} data than the CFA^{-1}

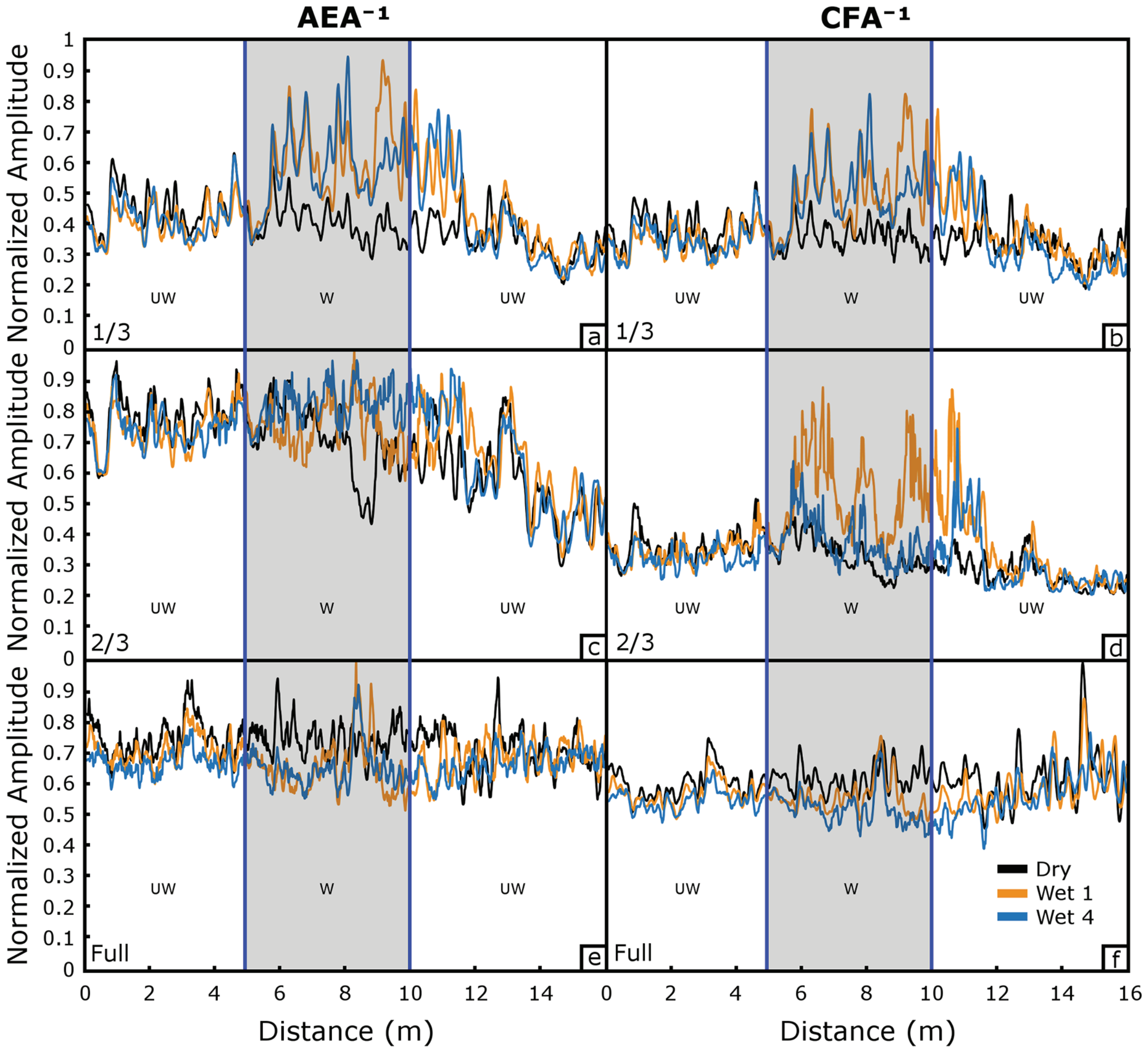

Fig. 7. Experiment 2 early-time ground-penetrating radar data showing time window comparison for 1000 MHz data. Uphill is to the right. All values are normalized so that the maximum value for that graph is 1. The shaded area is the wetted area, additionally marked "W"; the unwetted area is marked "UW." "1/3" represents the first one-third of the first positive half cycle (FPHC); "2/3" represents the first two-thirds of the FPHC; "Full" represents analysis of the entire FPHC. Black, background data; gold, first irrigation; blue, fourth and final irrigation. Data from second and third irrigations were omitted for clarity. AEA^{-1} and CFA^{-1} are the inverse of the average envelope amplitude and the carrier frequency amplitude, respectively.

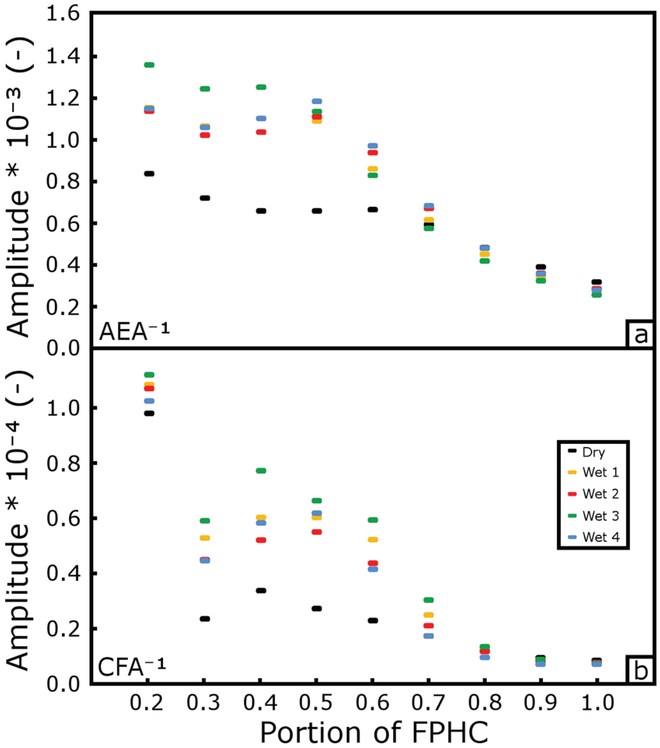

Fig. 8. Experiment 2 early-time ground-penetrating radar data analyzed based on nine different time windows ranging from 20 to 100% of the first positive half cycle (FPHC). Early-time signal (ETS) amplitude is plotted against time window size, with background data and all four irrigations shown. The ETS values are a single average value based on the entire irrigated portion of the line for that irrigation. AEA^{-1} and CFA^{-1} are the inverse of the average envelope amplitude and the carrier frequency amplitude, respectively.

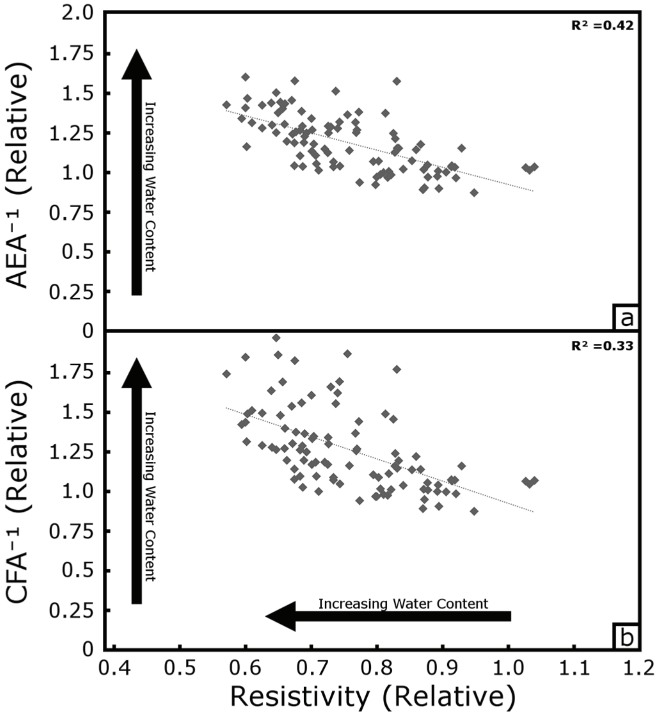

Fig. 9. Correlation of the 250 MHz ground-penetrating radar inverse of the average envelope amplitude (AEA^{-1}) (a) and inverse of the carrier frequency amplitude (CFA^{-1}) (b) data from Exp. 1 with the inversion-derived resistivity values from 12.5 cm deep using ground-penetrating radar and electrical resistivity imaging data from each irrigation presented as relative change from their associated background (dry) values. Only data from the irrigated region (5–10 m) are analyzed. Linear least squares regression and associated R^2 values are plotted. FPHC, first positive half cycle.

results, which exhibit a greater degree of change in response to each irrigation. The 20% analysis of CFA^{-1} has significantly higher values than the subsequent time windows, whereas this effect is less pronounced in the AEA^{-1} data. For both statistics, the Wet 4 values decrease from the Wet 3 values for most time windows.

Early-Time Signal Correlation with Changes in Resistivity

The soil core GWC measurements proved to be spatially too sparse to offer a good comparison with GPR. The ERI provided a more reliable dataset for correlation, with 32 estimates of resistivity changes within the irrigated portion of the transect (although subject to spatial regularization from the inversion of the ERI data). The AEA^{-1} and CFA^{-1} 250 MHz data, presented as values relative to background, from Exp. 1 correlate negatively with changes in ERI (Fig. 9), as expected: lower relative resistivity represents a wetter subsurface, which should result in higher ETS values. The AEA^{-1} data ($R^2 = 0.42$) have a better correlation with the ERI data than do the CFA^{-1} data ($R^2 = 0.33$). The other frequencies, which experienced potential interference issues in Exp. 1, do not correlate well. In Exp. 2, neither the AEA^{-1} nor the CFA^{-1} calculated from the 1000 MHz GPR data correlated well with the ERI values.

Discussion

The gravimetric analysis of soil cores (Fig. 3) combined with the ERI results (Fig. 4) confirm that the irrigation caused sufficient changes to subsurface moisture content to permit the performed analysis of the ETS. Specifically, these results show that we irrigated the desired portion of the ETS survey line, both laterally and vertically, by the final irrigation. The ERI data also show that the irrigation water infiltrated primarily into the targeted area of the line and was distributed throughout the 5-m length of the irrigation area. Soil sampling and subsequent GWC analysis confirmed that the irrigation significantly influenced the moisture content profile over the depth range of the expected sensitivity of the ETS, although the increase in GWC is not as consistent as would be expected based on ERI results. This may be due to the limited number of soil samples and the relatively small volume they represent, compared with the ERI dataset. Although there are only seven soil cores in Exp. 1 and six soil cores in Exp. 2, the ERI data, which were collected with a 32-cm electrode spacing, provide a greater number of samples and a larger sampling volume along the entire length of the GPR transect.

Comparison of Antenna Frequencies Using Experiment 1 Data

With the notable exception of the 1000 MHz CFA^{-1}, and to an extent the 1000 MHz AEA^{-1} data, which increases after the first irrigation event and does not respond to further irrigation, results from Exp. 1 show that CFA^{-1} and AEA^{-1} respond to changing moisture content, as expected, over multiple frequencies (Fig. 5). The AEA^{-1} and CFA^{-1} statistics increase in response to irrigation, excluding the 1000 MHz CFA^{-1} data, which decreases. Higher-frequency ETS data show more small-scale variability. This is expected due to the inverse relationship between frequency and depth of investigation; higher frequency antennae are sensitive to a smaller portion of the subsurface and are therefore more affected by small-scale heterogeneity in the subsurface. This suggests that measurement inconsistencies, such as changes in ground coupling caused by surface roughness, vegetative cover, small-scale subsurface heterogeneity, and preferential flow, may have a greater negative impact on the signal-to-noise ratio of high-frequency ETS data.

In the case of both AEA^{-1} and CFA^{-1}, the 250 MHz ETS data change in response to each of the three irrigations. However, there is a difference between AEA^{-1} and CFA^{-1} in the 400 MHz data. The AEA^{-1} statistic increases after the first irrigation but shows no further increase beyond this level. The CFA^{-1} statistic, on the other hand, increases a similar amount with each irrigation and, like the 250 MHz data, does not appear to lose sensitivity to moisture content increases after the first irrigation. One explanation for this is that CFA^{-1} is tied to changes in electromagnetic properties over a wider range of values than AEA^{-1}, which would be in line with the findings of Comite et al. (2016).

The 1000 MHz AEA^{-1} and CFA^{-1} data both decrease in response to irrigation. This anomalous result is a possible result of interference with the reflected signal from the infiltration front (Fig. 6) and is discussed further in the analysis of Exp. 2 below.

Post-Processing Effects on Experiment 2 Data

To carry out our spatial GPR analysis for the 1000 MHz dataset acquired in Exp. 2, we calculated the AEA^{-1} and CFA^{-1} based on three different time windows (Fig. 7) rather than just the single time window (i.e., the FPHC) commonly used to calculate the statistics for Exp. 1. We calculated both ETS statistics for the first one-third of the FPHC, the first two-thirds of the FPHC, and the entire FPHC (the standard approach). Although both AEA^{-1} and CFA^{-1} show the expected change in response to irrigation for the first one-third of the FPHC, the correlation is less consistent when analyzing the first two-thirds of the FPHC. Both statistics, when calculated using the full FPHC time window, decrease in response to irrigation. This behavior is counter to previous experimental results and numerical modeling (DiMatteo et al., 2013). These data suggest that, at some time after the first third of the FPHC, a source of interference appears in the GPR signal. This may be caused by a shallow wetting front induced by our irrigation-producing shallow reflectors (Fig. 6). Early-time signal analysis of the modeled traces shows a significant drop in the AEA^{-1} and CFA^{-1} statistics for a 1000 MHz antenna in the presence of a reflector 1 cm beneath the surface (Table 2). This is similar to the unexpected results in our 1000 MHz data in Exp. 1. These results indicate that caution is warranted when selecting a time window for ETS analysis. Although it has previously been proposed that the FPHC of the GPR signal provides the best signal-to-noise ratio for ETS analysis (DiMatteo et al., 2013), our data show that this may not always be the case.

To further investigate these effects, we analyzed smaller time windows, ranging from 20 to 100% in 10% increments, and calculated the average of the AEA^{-1} and CFA^{-1} values collected within the irrigated area for each irrigation (Fig. 8). The dry values are consistent from 20 to 60% for AEA^{-1} and from 30 to 60% for CFA^{-1}. Beginning at 70% of the FPHC, the AEA^{-1} data decrease ~0.1 with each additional 10% for both the dry and irrigated data (Fig. 8a). This is likely due to signal interference. In general, for the time windows that seem to provide robust data, both ETS statistics increase from background values in response to the first irrigation, remain the same or decrease slightly after the second irrigation, increase uniformly in response to the third irrigation, and decrease after the fourth irrigation for most time windows. These changes are most apparent in the CFA^{-1} values, which exhibit larger changes than the AEA^{-1} values. This confirms our finding in Exp. 1 (i.e., that CFA^{-1} is more sensitive over a wider range of conditions than the AEA^{-1}). However, the AEA^{-1} appears to provide quality information for a wider range of time windows than CFA^{-1}. The statistics do not respond to irrigation events as expected, but the ERI and soil sampling data also do not show a perfect stepwise GWC increase in response to each irrigation. Thus, the observed dynamics may be a hydrological phenomenon rather than inaccuracy in the GPR data.

Early-Time Signal–Electrical Resistivity Imaging Correlation Analysis

In Exp. 2, the 1000 MHz GPR ETS metrics increase significantly after the first irrigation but do not respond significantly to subsequent irrigations. The Exp. 2 ERI data respond similarly. Because neither set of values change significantly, they do not provide a useful correlation. The 250 MHz AEA^{-1} and CFA^{-1} values from Exp. 1, on the other hand, increase incrementally with each irrigation and correlate well with the associated ERI data. The AEA^{-1} correlation with ERI has an R^2 value of 0.42, whereas the CFA^{-1} correlation has an R^2 value of 0.33. The analysis in Fig. 9 demonstrates that there is a statistically significant negative relationship (p value well under 0.001) between the normalized ETS and ERI data. This demonstrates that a relationship could potentially be developed to relate ETS amplitude values to soil moisture content at the field scale. Although the AEA^{-1} provided a better correlation in this instance, it would be unwise to draw conclusions about the relative value of the AEA^{-1} and CFA^{-1} for field calibration from this single correlation analysis.

Conclusion

This field-scale irrigation experiment further confirms the viability of both the AEA^{-1} and CFA^{-1} statistics determined from

GPR ETS analysis for monitoring changes in soil moisture content under field conditions. Although AEA^{-1} provided useful information over a wider range of time windows, CFA^{-1} was better than AEA^{-1} at responding to changes over a wide range of moisture contents. In our 400 MHz dataset from Exp. 1, CFA^{-1} increased in response to each irrigation. Although AEA^{-1} increased in response to the first irrigation, it did not increase further with subsequent irrigations. Experiment 2, in which we performed an ETS analysis using different-sized portions of the FPHC as the time window, suggests that the 1000 MHz ETS data were influenced by a shallow reflector, such as the irrigation wetting front. This hypothesis is further supported by a synthetic model for a scenario where the reflection from a shallow wetting front interferes with the GPR FPHC. Thus, in cases where a shallow reflector is present, the FPHC may not be the optimal time window for ETS analysis. The style of plot shown in Fig. 8 can provide insight into which time windows provide high-quality data for a particular dataset. We also find a reasonable and statistically significant linear relationship between our 250 MHz GPR and ERI data from Exp. 1, indicating that the changes in ETS values are related to changes in soil moisture content. When used with an understanding of the field site, ETS analysis of GPR data can provide useful information on the dielectric properties of the shallow subsurface.

Acknowledgments

We thank Rhys Ashton (Rothamsted Research) and Tuvia Turkletaub (Lancaster University) for assistance in the field; Michael Tso (Lancaster University) for assistance with data analysis; and the reviewers, including Dr. Adam Mangel, for their invaluable and thoughtful comments and revisions. Funding for this research was provided by a travel award to Jonathan Algeo from the Rutgers Center for Global Advancement and International Affairs (GAIA). Woburn Experimental Farm is run by Rothamsted Research and is funded by UK Biotechnology and Biological Sciences Research Council (BBSRC).

References

Algeo, J., R.L. Van Dam, and L. Slater. 2016. Early-time GPR: A method to monitor spatial variations in soil water content during irrigation in clay soils. Vadose Zone J. 15.11. doi:10.2136/vzj2016.03.0026

Allroggen, N., N.L.M.B. van Schaik, and J. Tronicke. 2015. 4D ground-penetrating radar during a plot scale dye tracer experiment. J. Appl. Geophys. 118:139–144. doi:10.1016/j.jappgeo.2015.04.016

Annan, A.P. 1973. Radio interferometry depth sounding: I. Theoretical discussion. Geophysics 38(3):557–580. doi:10.1190/1.1440360

Binley, A. 2015. Tools and techniques: DC electrical methods. In: G Schubert, editor, Treatise on geophysics. 2nd ed. Vol. 11. Elsevier, New York. p. 233–259. doi:10.1016/B978-0-444-53802-4.00192-5

Binley, A., S.S. Hubbard, J.A. Huisman, A. Revil, D.A. Robinson, K. Singha, and L.D. Slater. 2015. The emergency of hydrogeophysics for improved understanding of subsurface processes over multiple scales. Water Resour. Res. 51:3837–3866.

Catt, J.A., D.W. King, and A.H. Weir. 1975. The soils of Woburn Experimental Farm I. Great Hill, Road Piece and Butt Close. Rothamsted Experimental Station Report for 1974 Part 2. FAO, Rome.

Comite, D., A. Galli, C. Ferrara, S.E. Lauro, E. Mattei, G. Vannaroni, and E. Pettinelli. 2014. Numerical and experimental surveys on the GPR early-time signal features for the evaluation of shallow-soil permittivity. In: Proceedings of the 15th International Conference on Ground Penetrating Radar, Brussels, Belgium. 30 June–4 July 2014. IEEE, New York. p. 131–134. doi:10.1109/ICGPR.2014.6970400

Comite, D., A. Galli, S.E. Lauro, E. Mattei, and E. Pettinelli. 2016. Analysis of GPR early-time signal features for the evaluation of soil permittivity through numerical and experimental surveys. IEEE J. Sel. Top. Appl. Earth Obs. Remote Sens. 9(1):178–187. doi:10.1109/JSTARS.2015.2466174

Di Matteo, A., P. Elena, and S. Evert. 2013. Early-time GPR signal attributes to estimate soil dielectric permittivity: A theoretical study. IEEE Trans. Geosci. Remote Sens. 51:1643–1654. doi:10.1109/TGRS.2012.2206817

Du, S. 1996. Determination of water content in the subsurface with the ground wave of ground penetrating radar. Ph.D. diss. Ludwig-Maximilians-Univ., Munich, Germany.

Ferrara, C., P.M. Barone, C.M. Steelman, E. Pettinelli, and A.I. Endres. 2013a. Monitoring shallow soil water content under natural field conditions using the early-time GPR signal technique. Vadose Zone J. 12(4). doi:10.2136/vzj2012.0202

Ferrara, C., V. Di Tullio, P.M. Barone, E. Mattei, S.E. Lauro, N. Proietti, et al. 2013b. Comparison of GPR and unilateral NMR for water content measurements in a laboratory scale experiment. Near Surf. Geophys. 11:143–153. doi:10.3997/1873-0604.2012051

Galagedara, L.W., G.W. Parkin, and J.D. Redman. 2003. An analysis of the ground-penetrating radar direct ground wave method for soil water content measurement. Hydrol. Processes 17:3615–3628. doi:10.1002/hyp.1351

Grote, K., S. Hubbard, and Y. Rubin. 2003. Field-scale estimation of volumetric water content using ground-penetrating radar ground wave techniques. Water Resour. Res. 39:1321. doi:10.1029/2003WR002045

Holden, P.A., and N. Fierer. 2005. Microbial processes in the vadose zone. Vadose Zone J. 4:1–21. doi:10.2136/vzj2005.0001

Huisman, J.A., S.S. Hubbard, J.D. Redman, and A.P. Annan. 2003. Measuring soil water content with ground penetrating radar. Vadose Zone J. 2:476–491. doi:10.2136/vzj2003.4760

IUSS Working Group WRB. 2015. World reference base for soil resources 2014, update 2015: International soil classification system for naming soils. World Soil Resour. Rep. 106. FAO, Rome.

Klute, A. 1965. Laboratory measurement of hydraulic conductivity of saturated soil. In: C.A. Black, editor, Methods of soil analysis. Part 1. Physical and mineralogical properties, including statistics of measurement and sampling. Agron. Monogr. 9. ASA and SSSA, Madison, WI. p. 210–221. doi:10.2134/agronmonogr9.1.c13

Mangel, A.R., S.M.J. Moysey, J.C. Ryan, and J.A. Tarbutton. 2012. Multi-offset ground penetrating radar imaging of a lab-scale infiltration test. Hydrol. Earth Syst. Sci. 16:4009–4022. doi:10.5194/hess-16-4009-2012

Nielsen, D.R. 1986. Water flow and solute transport processes in the unsaturated zone. Water Resour. Res. 22(9S):89S–108S. doi:10.1029/WR022i09Sp0089S

Pettinelli, E., A. Di Matteo, S.E. Beaubien, E. Mattei, S.E. Lauro, A. Galli, and G. Vannaroni. 2014. A controlled experiment to investigate the correlation between early-time signal attributes of ground-coupled radar and soil dielectric properties. J. Appl. Geophys. 101:68–76. doi:10.1016/j.jappgeo.2013.11.012

Pettinelli, E., G. Vannaroni, B. Di Pasquo, E. Mattei, A. Di Matteo, A. De Santis, and A.P. Annan. 2007. Correlation between near-surface electromagnetic soil parameters and early-time GPR signals: An experimental study. Geophysics 72(2):A25–A28. doi:10.1190/1.2435171

Sbartaï, Z.M., S. Laurens, J.-P. Balayssac, G. Arliguie, and G. Ballivy. 2006. Ability of the direct wave of radar ground-coupled antenna for NDT of concrete structures. NDT Int. 39:400–407. doi:10.1016/j.ndteint.2005.11.003

Seneviratne, S.I., T. Corti, E.L. Davin, M. Hirschi, E.B. Jaeger, I. Lehner, et al. 2010. Investigating soil moisture-climate interactions in a changing climate: A review. Earth Sci. Rev. 99:125–161. doi:10.1016/j.earscirev.2010.02.004

Sperl, C. 1999. Determination of spatial and temporal variation of the soil water content in an agro-ecosystem with ground-penetrating radar. Ph.D. diss. Technische Univ. München, Munich, Germany.

Steelman, C.M., and A.L. Endres. 2010. An examination of direct ground wave soil moisture monitoring over an annual cycle of soil conditions. Water Resour. Res. 46:W11533. doi:10.1029/2009WR008815

van Overmeeren, R.A., S.V. Sariowan, and J.C. Gehrels. 1997. Ground penetrating radar for determining volumetric soil water content: Results of comparative measurements at two test sites. J. Hydrol. 197:316–338. doi:10.1016/S0022-1694(96)03244-1

Warren, C., A. Giannopoulos, and I. Giannakis. 2016. gprMax: Open source software to simulate electromagnetic wave propagation for ground penetrating radar. Comput. Phys. Commun. 209:163–170. doi:10.1016/j.cpc.2016.08.020